

## Mineralogy and petrography of the Almahata Sitta ureilite

Michael ZOLENSKY<sup>1\*</sup>, Jason HERRIN<sup>2</sup>, Takashi MIKOUCHI<sup>3</sup>, Kazumasa OHSUMI<sup>4</sup>,  
Jon FRIEDRICH<sup>5</sup>, Andrew STEELE<sup>6</sup>, Douglas RUMBLE<sup>6</sup>, Marc FRIES<sup>7</sup>, Scott SANDFORD<sup>8</sup>,  
Stefanie MILAM<sup>9</sup>, Kenji HAGIYA<sup>10</sup>, Hiroshi TAKEDA<sup>3</sup>, Wataru SATAKE<sup>3</sup>, Taichi KURIHARA<sup>3</sup>,  
Matthew COLBERT<sup>11</sup>, Romy HANNA<sup>11</sup>, Jessie MAISANO<sup>11</sup>, Richard KETCHAM<sup>11</sup>,  
Cyrena GOODRICH<sup>12</sup>, Loan LE<sup>2</sup>, GeorgAnn ROBINSON<sup>2</sup>, James MARTINEZ<sup>2</sup>, Kent ROSS<sup>2</sup>,  
Peter JENNISKENS<sup>13</sup>, and Muawia H. SHADDAD<sup>14</sup>

<sup>1</sup>ARES, NASA Johnson Space Center, Houston, Texas 77058, USA

<sup>2</sup>ESCG Jacobs, Houston, Texas 77058, USA

<sup>3</sup>Department of Earth and Planetary Science, University of Tokyo, Bunkyo-ku, Tokyo 113-0033, Japan

<sup>4</sup>JASRI, Sayo-cho, Hyogo 679-5198, Japan

<sup>5</sup>Department of Chemistry, Fordham University, Bronx, New York 10458; Department of Earth and Planetary Sciences,  
American Museum of Natural History, New York, New York 10024, USA

<sup>6</sup>Geophysical Laboratory, Carnegie Institution of Washington, Washington, District of Columbia 20015, USA

<sup>7</sup>Jet Propulsion Laboratory, M/S 183-301, 4800 Oak Grove Drive, Pasadena, California 91109, USA

<sup>8</sup>NASA Ames Research Center, Moffett Field, California 94035, USA

<sup>9</sup>NASA Goddard Space Flight Center, Greenbelt, Maryland 20771, USA

<sup>10</sup>Graduate School of Life Sciences, University of Hyogo, Kamigori-cho, Hyogo 678-1297, Japan

<sup>11</sup>University of Texas High-Resolution X-ray CT Facility, University of Texas, Austin, Texas 78712, USA

<sup>12</sup>Planetary Science Institute, Tucson, Arizona 85719, USA

<sup>13</sup>SETI Institute, Mountain View, California 94043, USA

<sup>14</sup>Physics and Astronomy Department, University of Khartoum, Khartoum 11115, Sudan

\*Corresponding author. E-mail: michael.e.zolensky@nasa.gov

(Received 19 February 2010; revision accepted 01 October 2010)

---

**Abstract**—We performed a battery of analyses on 17 samples of the Almahata Sitta meteorite, identifying three main lithologies and several minor ones present as clasts. The main lithologies are (1) a pyroxene-dominated, very porous, highly reduced lithology, (2) a pyroxene-dominated compact lithology, and (3) an olivine-dominated compact lithology. Although it seems possible that all three lithologies grade smoothly into each other at the kg-scale, at the g-scale this is not apparent. The meteorite is a polymict ureilite, with some intriguing features including exceptionally variable porosity and pyroxene composition. Although augite is locally present in Almahata Sitta, it is a minor phase in most (but not all) samples we have observed. Low-calcium pyroxene (<5 mole% wollastonite) is more abundant than compositionally defined pigeonite; however, we found that even the low-Ca pyroxene in Almahata Sitta has the monoclinic pigeonite crystal structure, and thus is properly termed pigeonite. As the major pyroxene in Almahata Sitta is pigeonite, and the abundance of pigeonite is generally greater than that of olivine, this meteorite might be called a pigeonite-olivine ureilite, rather than the conventional olivine-pigeonite ureilite group. The wide variability of lithologies in Almahata Sitta reveals a complex history, including asteroidal igneous crystallization, impact disruption, reheating and partial vaporization, high-temperature reduction and carbon burning, and re-agglomeration.

---

## INTRODUCTION

On October 6, 2008, a small asteroid, 2008 TC<sub>3</sub>, was discovered and found to be on a collision course with Earth. Twenty hours later, 2008 TC<sub>3</sub> exploded at an unusually high, approximately 37 km, altitude over the Nubian Desert (due apparently to its weak physical constitution), and as a result the meteorites are spread over a large area. To date, four separate searches organized by coauthors Jenniskens and Shaddad have recovered approximately 600 stones of the Almahata Sitta (hereafter “Alma”) meteorite to date (Jenniskens et al. 2009). As we will describe here, Alma is a rather interesting ureilite, deserving of this short paper for reasons even aside from its remarkable recovery.

Although rare as falls, ureilites are the second most abundant achondrite group, after the HEDs (howardites, eucrites, and diogenites) (Hutchison 2004). Ureilites were originally defined as olivine-pigeonite achondrites (Mason 1962), but augite-bearing ureilites (Takeda et al. 1989) and orthopyroxene-pigeonite ureilites were found (Takeda 1989). Ureilites are generally coarse-grained bimineralic rocks, consisting almost entirely of olivine and pyroxene (Goodrich 1992; Scott et al. 1993; Mittlefehldt et al. 1998; Goodrich et al. 2004; Warren and Huber 2006; Downes et al. 2008). In this aspect, they resemble peridotitic rocks from Earth’s mantle. However, despite having residual mantle mineralogy, they have other characteristics that are difficult to reconcile with any simple igneous model, and the petrogenesis of ureilites remains highly controversial (Goodrich 1992; Mittlefehldt et al. 1998; Singletary and Grove 2003; Hudon et al. 2004; Warren and Huber 2006; Warren et al. 2006; Goodrich et al. 2007; Wilson et al. 2008; Warren 2010). Thus, it is of considerable interest that a new ureilite fall is now available for study and comparison.

We caution the reader that we have only had small masses available to us for this preliminary characterization, which is unfortunate because the large-scale textures of ureilites can be very difficult to determine from small, sub-cm sized chips. For example, one cannot well determine whether an ureilite has a large-scale poikilitic texture from such small samples (Goodrich 1992). Thus, it is possible that when larger masses are scrutinized a different picture of this meteorite may emerge.

## SAMPLES AND EXPERIMENTAL PROCEDURES

We analyzed chips from 17 different recovered definite Alma stones (stones 1, 4, 7, 15, 24, 29, 32, 36, 39, 44, 48, 49, 50, 51, 53, 54, and S138) (see Shaddad et al. 2010, for their masses and locations within the

strewn field). However, because of the brecciated nature of Alma and the limited masses of our samples (the subsamples we were allocated, with a single exception, weighed well under 1 g, many under 50 mg, and some were only individual mineral grains), we do not claim thoroughness. Of the samples we examined, only stone S138 weighed more than 1 g (it weighed 2.8 g). In this article, we report detailed results only for a subset of these samples, because the remainders are single mineral grains. There may well be other ureilite lithologies in Alma still waiting to be discovered among the approximately 580 samples we have not examined (!). We also briefly describe four non-ureilite meteorites (stones 16, 25, 41, and A100) found within the Alma strewn field. Although these stones may be unrelated to Alma, some evidence suggests that these and other non-ureilite stones found among the Alma strewn field are part of Alma (Shaddad et al. 2010; Sabbah et al. 2010; Kohout et al. 2010; Bischoff et al. 2010; Horstmann and Bischoff 2010).

Some Alma mineral compositions were determined using the Cameca SX100 microprobe at the E-beam laboratory of the Astromaterials and Exploration Science Directorate, Johnson Space Center, and others using the JEOL JXA-8900L microprobe at the University of Tokyo. We analyzed identical areas of Alma stone 7 to verify consistent results between these two instruments.

We attempted to collect single-crystal Laue patterns of individual crystals by the Laue synchrotron X-ray diffraction (SXRD) method using polychromatic synchrotron radiation at beamline BL-4B1 of the Photon Factory, National Laboratory for High Energy Accelerator Research Organization (KEK), Tsukuba, Japan. The Laue diffraction experiment was performed with the following conditions. The ring operated at 2.5 GeV. The exposure times were generally 30–60 min. We used polychromatic radiation at 0.3–3.0 Å. The beam size at the sample position was 1.6 μm in diameter, with a beam divergence of 40 μrad. These procedures are described in detail by Ivanov et al. (2000).

Electron backscatter diffraction (EBSD) pattern (Kikuchi diffraction pattern) analysis provides crystallographic and phase information of micrometer-sized crystalline materials prepared for observation in a scanning electron microscope (SEM) (Goehner and Michael 1996). Backscattered electrons (BSE) form an EBSD pattern on a phosphor screen distant from the specimen. The incident electrons are scattered mainly by phonons in the specimen with a large scattering angle and a small energy loss. These divergent electrons in the specimen are scattered again to form Kikuchi bands at certain angles. BSE images were taken using several

SEMs. We used a Hitachi S-4500 (field emission gun) SEM with Kevex energy-dispersive spectroscopy (EDS) at the Department of Earth and Planetary Sciences, University of Tokyo, Japan. This SEM is equipped with a ThermoNoran PhaseID EBSD detector, used for phase identification. The accelerating voltage of the incident beam was 20 kV with a beam current of 2–3 nA. The collection semiangle of the EBSD detector was approximately 37.5°. In the EBSD technique, the analyzed sections were tilted by approximately 70° from the horizontal toward a phosphor screen (detector) upon which BSE form an EBSD (Kikuchi) pattern. Calculations of Kikuchi patterns and analyses of observed EBSD patterns were performed using a computer program developed by Kogure (2003). We also used a cold field emission Hitachi S-4800 SEM at the Johnson Space Center. This SEM has an Oxford CHANNEL5 EBSD system with associated reduction software. Imaging and data reduction procedures were as above.

To assess mineral distributions, wavelength-dispersive spectroscopy (WDS) maps of elemental concentrations were acquired using the JEOL JXA 8900L electron microprobe (accelerating voltage, 15 kV; beam current, 120 nA) at the Department of Earth and Planetary Sciences, University of Tokyo, and also using the Cameca SX100 microprobe at the Johnson Space Center (described above). Quantitative WDS was also performed on a JEOL JXA 8900L electron microprobe (accelerating voltage, 15 kV; beam current, 12 nA), using well-characterized natural and synthetic standards.

Fragments of Alma stones 4 and 7 were examined by synchrotron X-ray computed microtomography (SXCT) at the GSECARS beamline 13-BM at the Advanced Photon Source of Argonne National Laboratory using techniques described in Friedrich et al. (2008). The entire fragment of stone 7 was imaged at a resolution of 13.5  $\mu\text{m}$  per voxel and a subsample of stone 4 was imaged at a resolution of 15.9  $\mu\text{m}$  per voxel. To assess the degree of collective preferred orientation of the high-Z (metal) phases in each, we used BLOB 3D (Ketcham 2005). With this package, a best-fit ellipsoid is digitally constructed around each individual grain and the direction of the major axis of each is plotted on an equal area, lower hemisphere stereo plot. With this, the collective degree of preferred orientation of individual grains can be visualized. Another product of these SXCT analyses was computed densities for stones 7 and 4.

In addition, two samples of Alma, a portion of stone 7 and the entirety of S138, were scanned at the University of Texas High-Resolution X-ray CT Facility (XCT) using the ACTIS scanner which in the ultrahigh-resolution mode yields maps of objects that can be

penetrated by relatively low-energy X-rays—in this case, a 225 kV microfocal X-ray source (Ketcham and Carlson 2001). The product XCT images were 1024  $\times$  1024 sixteen-bit TIFF images. Streak- and ring-removal processing of the images was based on correction of raw sinogram data using IDL routines “RK\_SinoDeStreak” and “RK\_SinoRingProcSimul,” both with default parameters (Ketcham 2005). The tomographic imaging was useful in identifying internal lithologic differences, pore and graphite distributions, and overall sample fabrics.

## RESULTS

### Petrography

After examining numerous, although small (generally subgram sized), samples of Alma (Table 1), we have identified three main lithologies. These are (1) a pyroxene-dominated, very porous, highly reduced lithology, (2) a pyroxene-dominated compact lithology, and (3) an olivine-dominated compact lithology. Although it seems possible that all three lithologies grade smoothly into each other at the kg-scale, at the g-scale this is not apparent. Thus, we will describe these three lithologies separately. We also describe several clasts found scattered within the major lithologies.

### Pyroxene-Dominated, Very Porous, Highly Reduced Lithology

The first analyzed Alma fragments (especially stone 7 and its subfragments 7-1 to 7-4) showed distinct color variability and streaking (Figs. 1 and 2). Alma stone 7 is the one originally described in Jenniskens et al. (2009), which is predominantly dark colored, but with lighter-colored streaks.

Despite the hue difference, both dark and light lithologies have a similar very porous, fine-grained polycrystalline texture, being mainly composed of mosaicized pyroxene and olivine with Fe-Ni metal and carbon phases. The abundance of pyroxene is higher than olivine in this lithology, giving it its name. Both olivine and pyroxene show granoblastic mosaic textures composed of 10–20  $\mu\text{m}$  grains, although rare crystals measuring up to 1 mm are present. The abundance of carbon phases and metal is variable, which probably explains the color differences. The texture is generally similar to that of mosaicized ureilites such as Haverö, Yamato-74154, and Allan Hills (ALH) 81101 (Fig. 1 shows mosaicism, although for Alma stone 1) (e.g., Berkley 1986). We note that the pyroxene-rich area in Alma stone 7 shows a similar mosaicized or mottled texture to olivine. However, while the olivine crystals

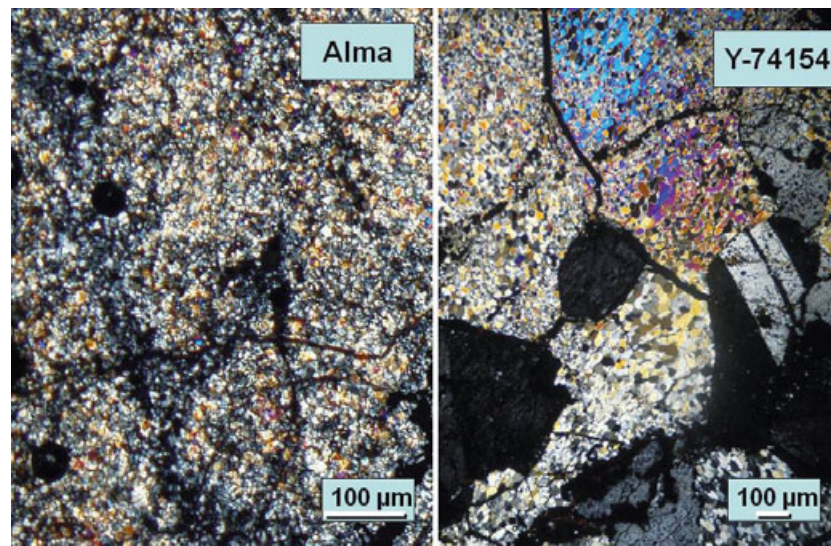


Fig. 1. Optical photomicrographs (cross-polarized light) of Alma stone 1 (left) and Y-74154 (right), both showing mosaiced texture. Note that Alma stone 1 shows a finer-grained texture than Y-74154 (note that the images are at different scales).

Table 1. Lithologies of the Almahata Sitta (Alma) samples in this investigation.

Stone	Major lithology	Comments
1	Pyroxene-dominated compact	See article for details
4	Pyroxene-dominated compact	See article for details
7	Pyroxene-dominated porous	See article for details
15	Pyroxene-dominated compact	See article for details
16	EL6 chondrite	Relationship to Alma unclear
24	Olivine-dominated compact	Small grain available; $\text{Fo}_{97-93}$ and $\text{En}_{52}\text{Wo}_6$
25	H5 chondrite	Relationship to Alma unclear
29	Uncertain	Only one small crystal available; $\text{En}_{72-71}\text{Wo}_{11}$
32	Uncertain	Only one small grain available; $\text{Fo}_{82-79}$
36	Uncertain	Only two crystals available: $\text{En}_{87}\text{Wo}_5$ and $\text{Fo}_{98-90}$
39	Pyroxene-dominated compact	See article for details
41	EH5 or EH6 chondrite	Relationship to Alma unclear
44	Olivine-dominated compact	Only one small grain available; $\text{Fo}_{84-79}$
48	Olivine-dominated compact	Only one small grain available; $\text{Fo}_{87-79}$
49	Uncertain	Only one small crystal available; $\text{Fo}_{79}$
50	Uncertain	Only one small crystal available; $\text{Fo}_{79}$
51	Uncertain	Only one small crystal available; $\text{En}_{82-83}\text{Wo}_9$
53	Porous lithology	Small grain available; $\text{Fo}_{86-79}$ and $\text{En}_{75-72}\text{Wo}_{7-6}$
54	Olivine-dominated compact	Only one small grain available; $\text{Fo}_{90-79}$
A100	L4 chondrite	Relationship to Alma unclear
S138	Olivine-dominated compact	See article for details

have been broken into domains with significantly varying extinction angles, under optical microscopy, the domains in pyroxenes have generally similar extinction angles, probably preserving original crystal orientation. While Alma stone 7 contains mainly pyroxene (~65 vol%), locally (as in subsample 7-3, which represented ~10% of our sample of stone 7) olivine predominates with only small amounts of pyroxene (~5 vol%) present as veins with widths of up to 200  $\mu\text{m}$ . At the boundary between olivine-rich and pyroxene-rich regions, pyroxene is present between

euhedral olivine grains. Pyroxene often shows twinning, probably on (100).

Olivine compositions in Alma 7 range from  $\text{Fo}_{92.4}$  to  $\text{Fo}_{83.6}$ , 0.13–0.92 wt% CaO, 0.25–0.6 wt%  $\text{Cr}_2\text{O}_3$ , and 0.39–0.58 wt% MnO (Table 2) (see Fig. 3, for a summary of olivine compositions from all Alma lithologies). Olivine adjacent to carbon typically displays the reverse zoning characteristic of ureilites, resulting from high-temperature reduction (Fig. 4). Olivine core (i.e., unreduced) compositions have a narrow range from  $\text{Fo}_{86.6}$  to  $\text{Fo}_{86.4}$  (Fig. 5). We

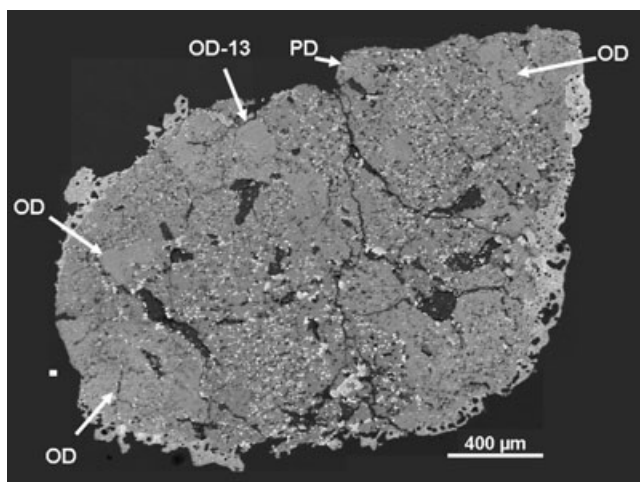


Fig. 2. BSE image of Alma stone 7, a pyroxene-dominated lithology with the highest porosity (up to 40%) and most extreme reduction textures. The large black areas are carbon, and the small black ones are pores. Metal and sulfide are white. Pyroxene and olivine are gray, principally the former. Fusion crust is present along the bottom, upper left, and right side of the section. It is evident that the highest porosities are associated with the highest concentration of metal and carbon, suggesting that the pores formed during high-temperature reduction. Closeups of this view are shown in later figures. “OD” indicates olivine-dominated clasts, and “OD-13” is the area shown in Fig. 14. “PD” indicates the pyroxene-dominated area shown in Fig. 15.

measured core compositions by making microprobe traverses across olivine grains in some instances, and by locating them using BSE images or element maps in others.

The very abundant pores in Alma 7 are present in both the olivine- and pyroxene-rich regions, but principally in the former. The pores have extremely irregular walls, which are lined with euhedral to subhedral olivine crystals (Fig. 6), and minor metal blebs. It is difficult to obtain good microprobe analyses of these olivines, because they do not often polish well, but the analyses we obtained are in the range  $\text{Fo}_{88-85}$ , very similar to the Alma groundmass olivine core compositions. X-ray tomography of stone 7 reveals that many of the pores define thin, discontinuous “sheets” connected in three dimensions, that may outline grains that have been incompletely welded together (Figs. 7 and 8).

Electron microprobe analysis shows that pyroxenes in Alma 7 are mostly low-Ca pyroxene with a rather wide compositional range (Fig. 9; Table 2). The low-Ca pyroxene in Alma stone 7 shows chemical zoning both in Mg-Fe and Ca ( $\text{En}_{90-80}\text{Wo}_{3-10}$ ) with Fe-rich low-Ca pyroxene cores and Mg-rich rims with higher Ca contents. Small amounts of augite (up to  $5\ \mu\text{m}$ ,  $\text{En}_{57}\text{Wo}_{40}$ ) are present associated with interstitial Si-rich

phases (Fig. 10). Alma 7 shows small variation in the Mg and Fe contents of the minute pyroxene crystals, but mm-scale heterogeneity is also present.

The mineralogy of this lithology is summarized in Table 3. Pyroxene crystal structures can provide important information on thermal history when coupled with chemical composition. Thus, we employed EBSD and SXRD to study the crystallography of Alma pyroxenes. Although the Ca contents of low-Ca pyroxenes are as low as  $\text{Wo}_2$ , the Kikuchi bands in the EBSD patterns show that all the Alma low-Ca pyroxenes we examined have a monoclinic space group ( $P2_1/c$ ) and crystal structure (Fig. 9). Despite the monoclinic symmetry, the Alma phase does not appear to be low-temperature clinoenstatite because the phases do not exhibit either kink banding, or consist of a fine mixture of lamellae of orthoenstatite and clinoenstatite, which are characteristic of low-temperature clinoenstatite (Deer et al. 1978, pp. 51–55; Tribaudino et al. 2003). Thus, we identify the mineral as pigeonite rather than low-temperature clinoenstatite. This result is unusual—generally a high Mg,  $\text{Wo}_2$  pyroxene would take either the ortho- or clinoenstatite structure, and, strictly speaking, “pigeonite” is defined as having  $\geq 5$  mole% Ca. A monoclinic structure is consistent with the observation that (100) twinning is common in these low-Ca clinopyroxenes. Adjacent pigeonites in stone 7 generally show a similar crystallographic orientation, as revealed by optical microscopy, indicating that they were once larger, continuous single crystals before some process (probably shock) produced mosaicism.

The EBSD Kikuchi bands from augite in Alma stone 7 can be best indexed by the  $C2/c$  augite structure, but we are not certain of the correctness of this structure because it is difficult to distinguish between the  $P2_1/c$  and  $C2/c$  pyroxene structures based solely on EBSD patterns, although augite appears to only crystallize with the space group  $C2/c$  (Mikouchi et al. 2010). EBSD was also performed on Alma olivine, and Kikuchi bands from all olivine grains analyzed could be indexed as the olivine structure, i.e., no high-pressure polymorph of olivine was indicated.

Aggregates of carbonaceous material are common in Alma 7, and measure up to 0.5 mm in width (Figs. 2, 8, 11, and 12). Confocal Raman imaging spectroscopy (CRIS) was conducted on small pieces of carbonaceous materials picked from a chip of Alma stone 7 (Steele et al. 2009; Ross et al., Forthcoming). CRIS combined with SEM imaging showed that the major carbon phase is highly crystalline graphite, some of which are flaky crystals. Raman spectra show the grains to be among the most graphitic of any meteorite yet studied with a G-band center and G-band full-width half max of  $1572 \pm 2.1$  and  $42 \pm 5\ \text{cm}^{-1}$  (Steele et al. 2009; Ross

Table 2. Compositions (wt%) of representative Almahata Sitta minerals, ordered by lithology.

(wt%)	Pyroxene-dominated compact lithology		Augite <sup>b</sup>		Pyroxene-dominated porous lithology		Pyroxene <sup>c</sup>		Olivine-dominated compact lithology		Pyroxene <sup>c</sup>		Olivine <sup>d</sup>		Pyroxene <sup>c</sup>		Olivine <sup>d</sup>	
	Olivine <sup>a</sup>	Olivine <sup>b</sup>	Pyroxene <sup>b</sup>	Augite <sup>b</sup>	Olivine <sup>c</sup>	Olivine <sup>c</sup>	Pyroxene <sup>c</sup>	Pyroxene <sup>c</sup>	Olivine <sup>d</sup>	Olivine <sup>d</sup>	Pyroxene <sup>c</sup>	Pyroxene <sup>c</sup>	Olivine <sup>d</sup>	Olivine <sup>d</sup>	Pyroxene <sup>c</sup>	Pyroxene <sup>c</sup>	Olivine <sup>d</sup>	Olivine <sup>d</sup>
SiO <sub>2</sub>	39.97	41.22	56.52	53.33	39.63	40.46	57.39	54.93	39.29	41.17	57.04	55.19						
TiO <sub>2</sub>	0.00	0.01	0.14	0.27	0.00	0.04	0.20	0.10	0.04	0.00	0.18	0.11						
Al <sub>2</sub> O <sub>3</sub>	0.02	0.03	1.01	1.71	0.08	0.59	1.46	1.48	0.04	0.02	1.32	0.88						
Cr <sub>2</sub> O <sub>3</sub>	0.62	0.40	1.03	1.32	0.68	0.40	0.20	0.10	0.40	0.77	0.92	1.18						
FeO	14.06	6.04	7.39	4.37	12.17	7.11	0.87	7.62	15.39	5.31	6.23	9.16						
MnO	0.48	0.52	0.61	0.44	0.49	0.43	0.34	0.36	0.48	0.57	0.39	0.40						
MgO	45.17	51.80	31.25	19.97	46.58	50.39	38.37	32.37	43.46	52.65	32.34	27.87						
CaO	0.14	0.29	2.53	18.41	0.33	0.32	0.40	2.27	0.36	0.34	3.10	5.21						
CoO	0.00	0.01	0.00	0.00	0.00	0.01	0.03	0.02	0.00	0.00	0.00	0.02						
NiO	0.00	0.02	0.04	0.02	0.00	0.07	0.00	0.06	0.05	0.00	0.03	0.00						
Na <sub>2</sub> O	0.01	0.00	0.03	0.23	0.01	0.02	0.04	0.09	0.02	0.00	0.01	0.08						
K <sub>2</sub> O	0.00	0.00	0.00	0.00	0.01	0.00	0.00	0.01	0.02	0.00	0.00	0.00						
P <sub>2</sub> O <sub>5</sub>	0.01	0.01	0.00	0.21	0.04	0.01	0.01	0.02	0.01	0.02	0.05	0.07						
S	0.01	0.00	0.01	0.00	0.01	0.00	0.00	0.01	0.00	0.00	0.00	0.07						
Total	100.34	100.36	100.56	100.27	99.99	99.88	99.44	99.85	99.98	100.76	100.51	100.17						
(wt%)	Metal <sup>b</sup>				Troilite <sup>c</sup>				Metal <sup>d</sup>				Troilite <sup>d</sup>					
Si	0.05				1.77			0.32					1.22					0.09
Ti	0.00				0.00			0.24					0.01					0.52
Al	0.32				0.02			0.02					0.00					0.02
Cr	0.05				0.09			8.99					0.03					3.51
Fe	95.94				93.84			50.83					90.56					57.54
Mn	0.01				0.00			0.91					0.00					0.76
Mg	0.00				0.01			0.28					0.01					0.02
Ca	0.06				0.02			0.02					0.00					0.04
Co	0.00				0.17			0.01					0.30					0.00
Ni	1.69				2.02			0.14					7.65					0.02
Na	0.00				0.00			0.00					0.00					0.00
K	0.00				0.00			0.00					0.00					0.00
P	0.60				0.29			0.00					0.44					0.00
S	0.01				0.02			38.16					0.02					37.76
Total	100.42				98.26			99.95					100.25					100.29

<sup>a</sup>Stone 1.<sup>b</sup>Stone 15.<sup>c</sup>Stone 7.<sup>d</sup>Stone S138.

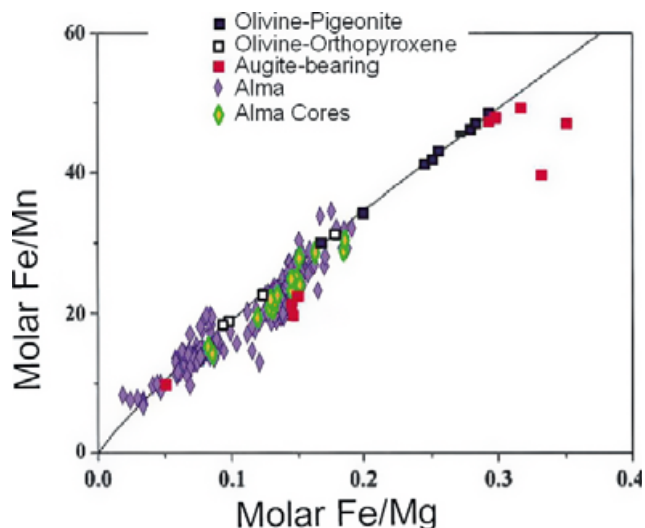


Fig. 3. Olivine analyses from five Alma samples (purple diamonds) plotted on a diagram of ureilite olivine molar Fe/Mn versus Fe/Mg adapted from Goodrich et al. (2004). Alma olivine cores are indicated by green and orange diamonds. The Alma olivines generally follow the chondritic Mn/Mg trend of main group olivine-pigeonite and olivine-orthopyroxene ureilites (the thin black line), with some displacements to the right consistent with the presence of a minor, augite-bearing component. Alma olivines largely separate into two fields, on either side of 0.1 Molar Fe/Mg, consistent with Alma's polymict nature. For each sample, the olivine core compositions lie to the right of the other compositions, reflecting higher relative Fe compositions consistent with reduction of the rims.

et al. Forthcoming). Diamond aggregates ranging up to several micrometers in dimension are contained within graphite grains. The microdiamonds are concentrated in small aggregates, which are clearly revealed and plucked out during polishing, leaving deep gouges across unlucky samples.

These carbon aggregates also contain fine-grained troilite and kamacite, the latter containing significant Si and P (up to 2.25 and 0.44 wt%, respectively). Fe-Ni metal is present in all Alma samples, and generally the largest masses are adjacent to carbon masses (Fig. 11). The metal has a narrow compositional range of  $\text{Fe}_{0.92}\text{Ni}_{0.08}$ – $\text{Fe}_{0.96}\text{Ni}_{0.04}$ . Troilite is widespread, but much less abundant than metal, and is principally found within the carbon aggregates. This troilite has significant Cr (up to 4.3 wt%), Mn, and Ti (Table 2).

One product of the SXCT imaging of stone 7 (which weighed  $\sim 1$  g) was a computed bulk, which was  $1.49 \text{ g cm}^{-3}$ . This is the lowest reliable bulk density ever measured for a meteorite, even lower than Tagish Lake, which has a bulk density of  $1.7 \text{ g cm}^{-3}$  (Zolensky et al. 2002). The tomographic study of Alma stone 7 also shows a distinct foliation based on the orientation of the metal grains present within it (Fig. 13).

## Clasts in Stone 7

Within Alma stone 7, we found two types of clasts consisting of minor lithologies displaying disparate textures and mineralogies. The boundaries of these clasts are generally abrupt, indicating that these are not merely gradational boundaries to the surrounding pigeonite-dominated lithology, and the mineralogical differences are too distinct for these clasts to be mere textural variants of stone 7. One clast lithology consists of fine-grained, porous to compact aggregates of olivine, generally with interstitial pigeonite, and local carbon and Fe-Ni metal (Fig. 14). In the example illustrated in Fig. 8, the olivine grains have the composition  $\text{Fo}_{87.6-85.3}$  and the interstitial pigeonite is  $\text{En}_{85}\text{Wo}_6$ – $\text{En}_{79}\text{Wo}_{13}$ . In these clasts, most olivine and pyroxene have interstitial silicates whose Si-content increases adjacent to metal grains (Herrin et al. 2009, 2010a, 2010b).

A very interesting type of clast consists entirely of rounded pyroxene grains containing abundant nanophase metal and minute domains of Ca-rich pyroxene (Fig. 15). SXRD reveals that these clasts consist mainly of well-crystalline pigeonite, and EPMA reveals that the rounded grains have a pigeonite composition. As the aggregates contain nanophase Fe metal grains which were included in the EPMA analyses, the true composition of this pigeonite must be more Mg-rich than is apparent. These rounded pigeonite grains are separated by thin (generally  $< 10 \mu\text{m}$ ) zones of silica, which is mostly amorphous, but is locally crystalline. We found, using EBSD, that the silica interstitial to the rounded pigeonite in these clasts ranges from amorphous to crystalline, but we were unable to identify definitively the silica phase. Some Kikuchi patterns were best indexed as cristobalite, whereas others were best indexed as tridymite.

## Pyroxene-Dominated, Compact Lithology

Alma stones 1, 4, 15, and 39 consist dominantly of a pyroxene-rich ( $> 50 \text{ vol}\%$ ), low porosity lithology (compact), with occasional olivine-rich regions (Figs. 16 and 17). In these samples, olivine is usually associated with the highest porosity.

The mineralogy of this lithology is summarized in Table 3. Pyroxene and olivine display an interlocking texture similar to that of typical main group ureilites (Mittlefehldt et al. 1998), with individual pyroxene crystals measuring up to  $500 \mu\text{m}$  and olivine up to  $200 \mu\text{m}$ . Pyroxenes in Alma 4 are clearly more Fe-rich ( $\text{En}_{85-78}\text{Wo}_{2-6}$ ) than those in Alma stone 7 (Fig. 9). In Alma stone 4 pyroxene, Fe and Ca are positively correlated. Olivine compositions in Alma 4 range from  $\text{Fo}_{93.1}$  to  $\text{Fo}_{86.9}$ , 0.25–0.70 wt% CaO, 0.46–0.66 wt%

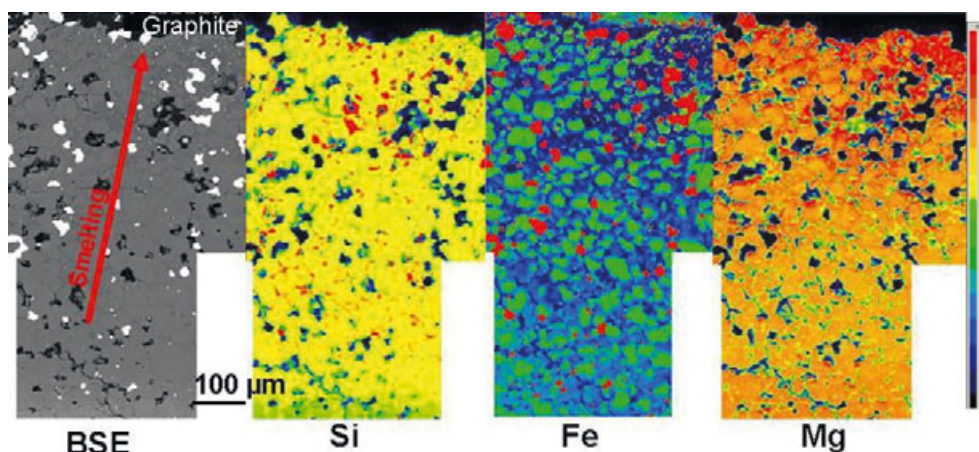


Fig. 4. X-ray element maps of stone 7, illustrating the chemical effects of smelting on an Alma lithology (in this case pyroxene-dominated porous). A piece of graphite lies at the top of the image, which drove the reduction, so that the degree of reduction increases toward the image top (along the arrow). In the Si map, red blebs are silica. In the Fe image, pigeonite is light blue to green, and metal is red. In the Mg map, pigeonite is orange through red, with Mg concentration being highest in red, where much of the Fe originally in pigeonite has been reduced to fine-grained Fe inclusions in low-Ca clinopyroxene.

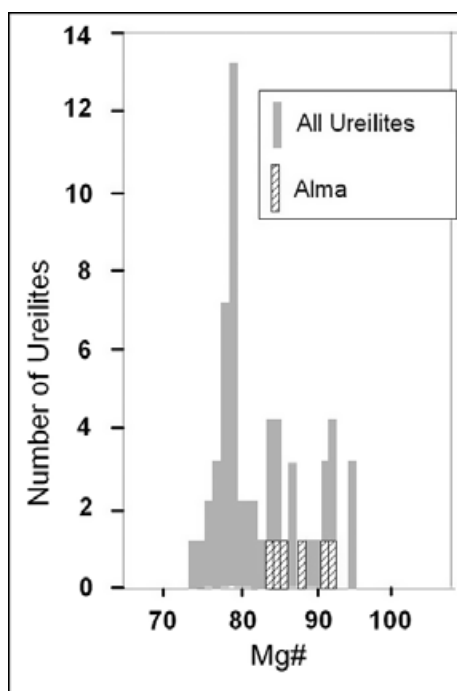


Fig. 5. Histogram of olivine core compositions (Mg#) for seven different Alma samples, compared to cores for monomict ureilites (from Mittlefehldt et al. 1998). The Alma olivine core compositions are generally distinct for each lithology.

$\text{Cr}_2\text{O}_3$ , and 0.50–0.66 wt% MnO (Table 2). Olivine core compositions range down to  $\text{Fo}_{86.9}$ .

Alma 39 looks like a fragment of a typical monomict (main group) ureilite, except for the low abundance of olivine. Pyroxenes in Alma 39 are all low-Ca pyroxene with a narrow compositional range

( $\text{En}_{74.8-74.2}\text{Wo}_{6.8-7.2}$ ) (Fig. 9). Olivine compositions in Alma 39 range from  $\text{Fo}_{95.9}$  to  $\text{Fo}_{78.5}$ , 0.19–0.44 wt% CaO, 0.25–0.91 wt%  $\text{Cr}_2\text{O}_3$ , and 0.33–0.54 wt% MnO. Olivine adjacent to carbon typically displays reverse zoning resulting from high-temperature reduction (Fig. 17). Olivine core (i.e., unreduced) compositions have a narrow range  $\text{Fo}_{82.3}$ – $\text{Fo}_{78.5}$  (Fig. 5).

Pyroxenes in Alma 15 include both low-Ca pyroxene with a narrow compositional range ( $\text{En}_{84.0-83.6}\text{Wo}_{5-4.8}$ ) and augite with a more variable composition ( $\text{En}_{57.6-54.9}\text{Wo}_{40.6-35.7}$ ). We did not determine the structural state of the low-Ca pyroxene. However, Goodrich et al. (2004) refer to pyroxenes of this range of Wo contents in ureilites as orthopyroxene, following the compositional definition (Deer et al. 1978). Thus, Alma 15 is similar to some olivine-augite-orthopyroxene main group ureilites (e.g., Goodrich et al. 2004). Takeda (1989) has proposed that there are distinct kinds of ureilite orthopyroxene with different origins, including primary orthopyroxene and another orthopyroxene inverted from primary pigeonite (inverted pigeonite). One type of primary orthopyroxene coexists with pigeonite (Takeda 1989) or with augite, or with pigeonite and augite (Takeda et al. 1989), and the secondary orthopyroxene inverted from pigeonite contains augite blebs produced during decomposition of pigeonite (Takeda et al. 2009). Thus, some of the above olivine-augite-orthopyroxene ureilites may be olivine-inverted pigeonite ureilites. Olivine compositions in Alma 15 range from  $\text{Fo}_{94.4}$  to  $\text{Fo}_{91.5}$ , 0.19–2.3 wt% CaO, 0.29–0.89 wt%  $\text{Cr}_2\text{O}_3$ , and 0.45–0.54 wt% MnO. Olivine adjacent to carbon typically displays reverse zoning resulting from high-temperature reduction.

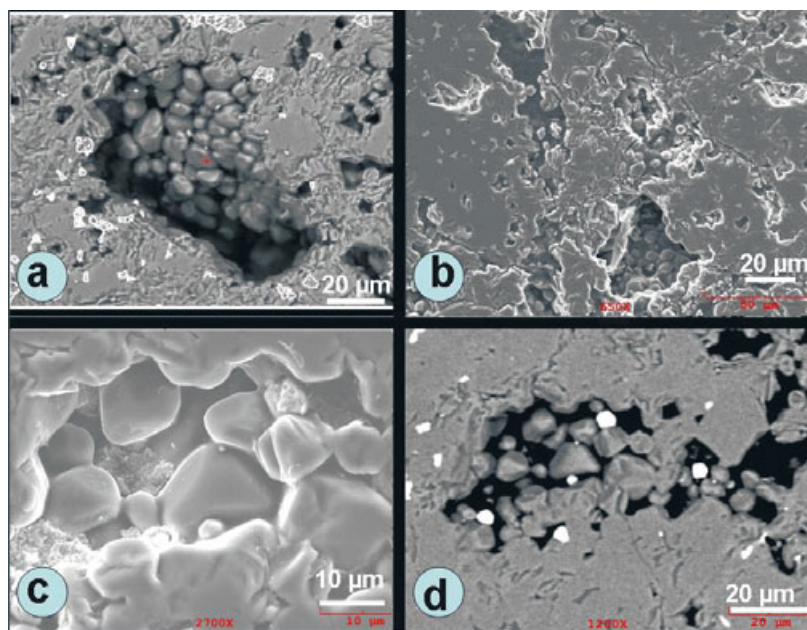


Fig. 6. a–c) SEI images of pores in olivine in Alma 7. The pore walls are completely covered by euhedral to subhedral crystals of olivine (principally), pyroxene, and metal. d) BSE image of a very irregular pore whose walls also feature the occasional metal grain (white).

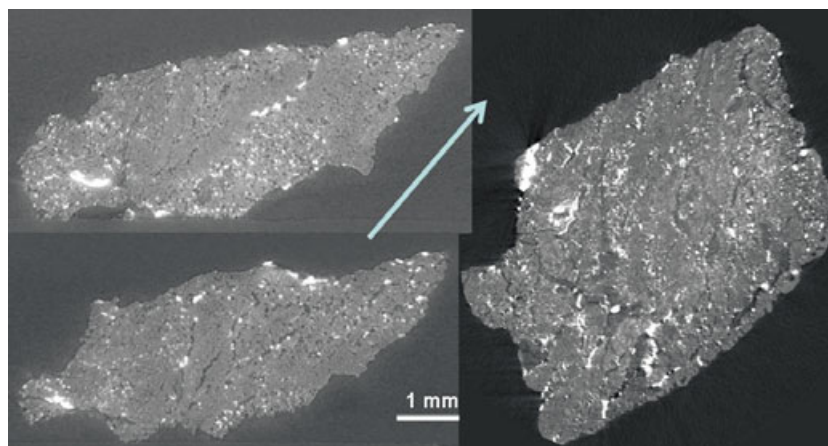


Fig. 7. CT tomographic images of a fragment of Alma stone 7. (Left) Two near-consecutive slices made using SXCT, indicating a slight fabric (arrow). In these computed images, carbon and pores all appear with equal contrast as dark gray to black, and metal and sulfides appear white. It is clear that there is a foliation defined by the carbon and pores, and it is easy to see that metal is proximal to carbon. (Right) XCT images of another fragment of Alma stone 7. In this computed image, there is better contrast between pores and carbon (see the following figure).

Pyroxenes in Alma 1 vary widely, including low-Ca pyroxene, pigeonite, and augite ( $\text{En}_{99-61}\text{Wo}_{1-37}$ ) (Fig. 9). Although the graphite in Alma mainly occurs as fine, flaky masses within the fine-grained aggregates, stones 4 and 39 contain large (up to 500  $\mu\text{m}$ ) apparently euhedral crystals of graphite (Figs. 12 and 16). The crystals are all blades, although this could be only a projection phenomenon, with random cuts through the hexagonal plates typical of graphite. Despite the euhedral appearance of these crystals, X-ray diffraction

patterns collected by SXRD display only diffuse diffraction maxima, indicating poor crystallinity. We do not know whether this is due to poor sample preparation, or to shock, although both explanations appear equally likely. However, the presence of euhedral-appearing graphite crystals in Alma is notable, because such grains are usually found only in ureilites of very low shock degree (Goodrich 1992; Mittlefehldt et al. 1998). This observation underscores the brecciated nature of Alma.

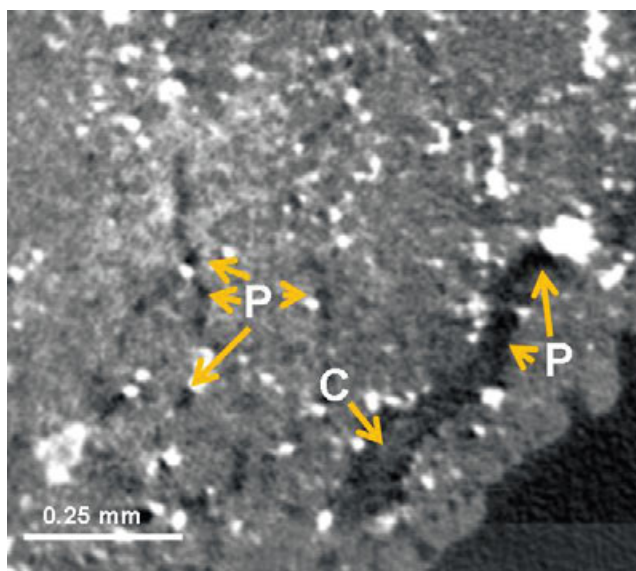


Fig. 8. Closeup of lower right portion of the XCT tomographic image from the previous figure. In this image, carbon (C—dark gray) is not always well-resolved from pores (P—black). Only a few of the pores are indicated in this image.

One subsample of stone 4 was imaged by SXCT, which resulted in a computed bulk density of  $3.08 \text{ g cm}^{-3}$ . This density is consistent with measured values for other ureilites (Britt and Consolmagno 2004), and is twice as high as that for Alma stone 7.

### Olivine-Dominated, Compact Lithology

We examined several samples of an olivine-dominated, compact lithology, especially stone S138 which at 2.8 g was the largest mass at our disposal (Fig. 18). Obviously, olivine is more abundant than pyroxene in this lithology. Stones 44, 48, and 54 appear to be the same lithology (Table 1), but since only a tiny grain of each sample was available for our study we cannot be certain of this conclusion. Alma A138 consists mainly of olivine, and lesser amounts of pigeonite. Carbon is less abundant than in stone 7, for example, and carbon masses are irregular to vein-like crystals, but not in well-defined crystals. Metal and troilite are present as in the other Alma lithologies.

Olivine compositions in Alma S138 range from  $\text{Fo}_{82.7}$  to  $\text{Fo}_{96.5}$ , 0.31–0.51 wt% CaO, 0.59–1.06 wt%  $\text{Cr}_2\text{O}_3$ , and 0.39–0.57 wt% MnO (Fig. 3; Table 2). Olivine adjacent to carbon typically displays the reverse zoning characteristic of ureilites, and pores and metal blebs are present (Fig. 4), all proposed to result from high-temperature reduction (Herrin et al. 2010b). Olivine core compositions have the narrow range  $\text{Fo}_{82.7}$ – $\text{Fo}_{83.0}$  (Fig. 5).

Electron microprobe analyses show that pyroxenes in Alma S138 are exclusively low-Ca pyroxene with a rather wide compositional range (Fig. 9). The pyroxene shows chemical zoning both in Mg-Fe and Ca ( $\text{En}_{75-85}\text{Wo}_{5-10}$ ) with the Fe-rich pyroxene cores ( $\text{En}_{75.3-75.8}\text{Wo}_{10.1-10.3}$ ) to the Mg-rich rims with lower Ca contents. We did not find augite in our survey of the S138 section.

### Non-ureilite Stones From the Alma Strewn Field

We briefly examined four very fresh (unweathered), fully fusion-crusts stones found within the Alma strewn field, and whose exact relationship to Alma, if any, is unknown. These stones are distinct, and represent four different chondrite types. All of the chips of these stones that we examined are monolithic, containing no other lithologies (including ureilite). The only terrestrial weathering that we could distinguish was minor oxidation of metal, to a degree that, in our experience, can occur after only a few days on Earth.

Stone 16 is a chondrite with abundant low-calcium pyroxene— $\text{En}_{95.7}\text{Wo}_{1.2}$  to  $\text{En}_{98.8}\text{Wo}_{0.8}$ , average  $\text{En}_{98.0}\text{Wo}_{1.0}$  ( $\text{CaO} \leq 0.63 \text{ wt\%}$ ,  $\text{MnO} \leq 0.03 \text{ wt\%}$ ). No olivine was found in the single small chip we examined. No chondrules are apparent. Accessory phases include kamacite (with  $\text{Si} \leq 1.24 \text{ wt\%}$ ), troilite, and ferroan alabandite. This meteorite is an EL6 chondrite.

Stone 25 is a chondrite with abundant olivine, and lesser low-calcium pyroxene. Olivine is  $\text{Fo}_{81.8}$ – $\text{Fo}_{82.3}$ , average  $\text{Fo}_{82.0}$  ( $\text{CaO} \leq 0.09 \text{ wt\%}$ ,  $\text{MnO} \leq 0.49 \text{ wt\%}$ ). Low-calcium pyroxene is  $\text{En}_{71.4}\text{Wo}_{0.2}$ – $\text{En}_{82.1}\text{Wo}_{1.2}$ . A few, poorly distinguished chondrules are apparent in the single small chip we examined. Accessory phases include diopside, kamacite, and troilite. This meteorite is an H5 chondrite.

Stone 41 is a chondrite with abundant low-calcium pyroxene— $\text{En}_{94.6}\text{Wo}_{0.5}$  to  $\text{En}_{98.4}\text{Wo}_{0.2}$ , average  $\text{En}_{96.8}\text{Wo}_{0.3}$  ( $\text{CaO} \leq 0.28 \text{ wt\%}$ ,  $\text{MnO} \leq 0.04 \text{ wt\%}$ ). No olivine was found in the single small chip we examined. No chondrules are apparent. Accessory phases include kamacite (with  $\text{Si} \leq 2.93 \text{ wt\%}$ ) and troilite. Stone 41 is an EH5 or EH6 chondrite.

Stone A100 is a chondrite with abundant olivine, and lesser low-calcium pyroxene. Olivine is  $\text{Fo}_{74.5}$ – $\text{Fo}_{76.4}$ , average  $\text{Fo}_{75.8}$  ( $\text{CaO} \leq 0.09 \text{ wt\%}$ ,  $\text{MnO} \leq 0.55 \text{ wt\%}$ ). Low-calcium pyroxene is  $\text{En}_{75.1}\text{Wo}_{1.0}$ – $\text{En}_{78.4}\text{Wo}_{3.0}$ , average is  $\text{En}_{77.2}\text{Wo}_{1.2}$ . Chondrules are abundant and very distinct in the single small chip we examined. Accessory phases include kamacite, taenite, and troilite. This meteorite is an L4 chondrite.

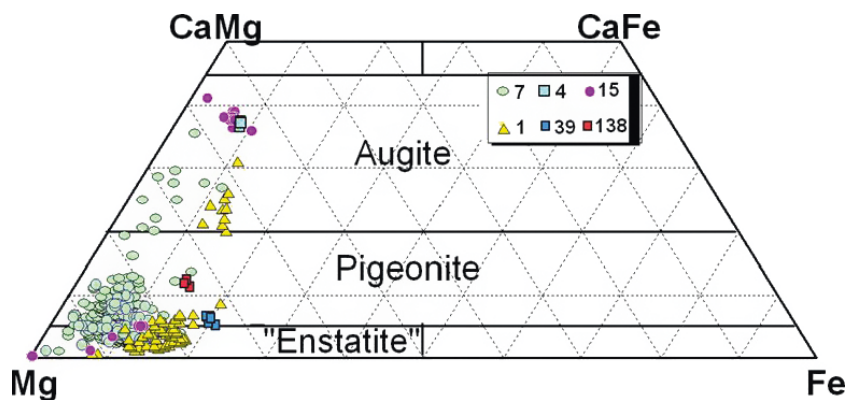


Fig. 9. Major element compositions of pyroxene (quadrilateral) in six of the studied Alma samples (stones 1, 4, 7, 15, 39, and S138). Despite the compositional range of low-Ca pyroxene in stone 7, these appear to all have the pigeonite crystal structure.

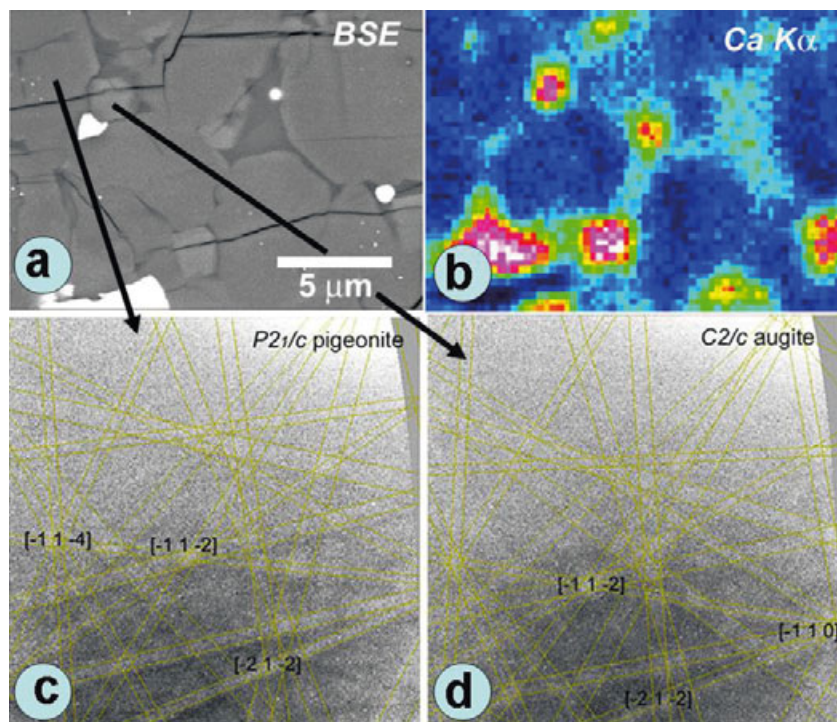


Fig. 10. a) BSE image of pyroxene-rich area in Alma 7. b) Corresponding Ca X-ray map. Dark blue is Fe-rich low-Ca pyroxene. Light blue is mostly Mg-rich pigeonite ( $\text{En}_{87}\text{Fs}_6\text{Wo}_7$ —Mg# is 0.936) with a high-Ca content. Augite is pink to white. Interstitial Si-rich phases are dark gray in the BSE image and black in the Ca map. c) EMSD pattern with Kikuchi bands of low-Ca pyroxene (white and gray) matching the calculated bands of the pigeonite  $P2_1/c$  structure (yellow). d) EBSD pattern with Kikuchi bands of high-Ca pyroxene (white and gray) matching the calculated bands of the augite  $C2/c$  structure (yellow).

## DISCUSSION

### Classification Issues

There are competing classification schemes for ureilites, reflecting the controversial nature of these meteorites, and we will mention three of these. Berkley et al. (1980) divided ureilites into groups based on Fo content of olivine. This classification was refined by Franchi et al. (1998). In this scheme, the samples of

Alma that we have studied belong to group II, although at the extreme upper limit Mg-rich value for this grouping. Alma olivine minor components (CaO, 0.1–0.65 wt%; MnO, 0.42–0.66 wt%; and  $\text{Cr}_2\text{O}_3$ , 0.24–0.81 wt%) are all consistent with this grouping.

Takeda et al. (1989) and Takeda (1989) proposed dividing recognized four groups of ureilites based on the pyroxene polymorphs: into olivine-pigeonite ureilites, olivine-orthopyroxene-pigeonite ureilites, olivine-orthopyroxene-augite ureilites, and olivine-inverted

Table 3. Summary of primary Almahata Sitta lithologies mineralogy.

Pyroxene-dominated porous lithology	
Mosaiced pyroxene and olivine, abundant pores	
Low-Ca pyroxene: $\text{En}_{90-80}\text{Wo}_{3-10}$	
High-Ca pyroxene: $\text{En}_{57}\text{Wo}_{40}$	
Olivine: $\text{Fo}_{92.4}\text{--}\text{Fo}_{83.6}$ , 0.13–0.92 wt% CaO, 0.25–0.6 wt% $\text{Cr}_2\text{O}_3$ , 0.39–0.58 wt% MnO	
Olivine cores: $\text{Fo}_{86.6}\text{--}\text{Fo}_{86.4}$	
Olivine in pores: $\text{Fo}_{88-85}$	
Fe-Ni metal: $\text{Fe}_{0.92}\text{Ni}_{0.08}\text{--}\text{Fe}_{0.96}\text{Ni}_{0.04}$	
Troilite, with significant Cr	
Graphite and diamond	
Pyroxene-dominated compact lithology	
Pores only locally abundant (generally associated with olivine)	
Low-Ca pyroxene: $\text{En}_{99-74.2}\text{Wo}_{1-7.2}$	
High-Ca pyroxene: $\text{En}_{57.6-54.9}\text{Wo}_{40.6-35.7}$	
Olivine: $\text{Fo}_{95.9}\text{--}\text{Fo}_{86.9}$ , 0.19–0.70 wt% CaO, 0.25–0.91 wt% $\text{Cr}_2\text{O}_3$ , 0.33–0.66 wt% MnO	
Olivine cores: $\text{Fo}_{86.9}\text{--}\text{Fo}_{86.4}$	
Fe-Ni metal	
Troilite, with significant Cr	
Graphite and diamond	
Olivine-dominated compact lithology	
Pores only locally abundant (generally associated with olivine)	
Olivine: $\text{Fo}_{82.7}\text{--}\text{Fo}_{96.5}$ , 0.31–0.51 wt% CaO, 0.59–1.06 wt% $\text{Cr}_2\text{O}_3$ , 0.39–0.57 wt% MnO	
Olivine cores: $\text{Fo}_{82.7}\text{--}\text{Fo}_{83.0}$	
High-Ca pyroxene: $\text{En}_{75-85}\text{Wo}_{5-10.3}$	
Pyroxene cores: $\text{En}_{75.3-75.8}\text{Wo}_{10.1-10.3}$	
Fe-Ni metal	
Troilite, with significant Cr	
Graphite and diamond	

pigeonite ureilites. In contrast to this plan, Goodrich et al. (2004) divided ureilites into three groups based on mineralogy: olivine-pigeonite, olivine-orthopyroxene, and augite-bearing. Note that in this scheme, the distinction between pigeonite and orthopyroxene is defined compositionally ( $\text{Wo} > 5$  versus  $\text{Wo} \leq 5$ , respectively) rather than structurally (Deer et al. 1978). Although we do not choose one ureilite classification scheme over another, for the purposes of this discussion we will use Goodrich's and leave it to the reader to make his or her own decision. According to Goodrich's classification, Alma #15 is an augite-bearing ureilite, whereas all others are olivine-orthopyroxene or olivine-pigeonite. We emphasize, however, that our structural studies show that most low-Ca pyroxenes in Alma are pigeonite. In addition, as the abundance of low-Ca pyroxene is generally much greater than that of olivine in these samples, we suggest that the order of terms should be reversed (e.g., pigeonite-olivine rather than olivine-pigeonite). In terms of igneous rock

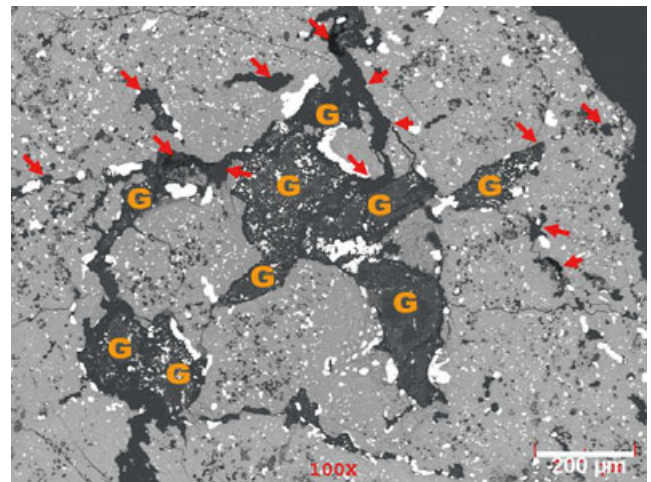


Fig. 11. High magnification BSE image of carbon aggregates in Alma 7, which are labeled “G” (for graphite), in association with large pores (arrowed). This image also makes manifest the association of metal (white) with the carbon, which suggests that metal is largely (at least) a reduction product.

classification, most of the Alma samples we have studied would be most similar to terrestrial wehrlites.

In terms of igneous rock classification, Almahata Sitta would be most similar to terrestrial wehrlites.

#### Mineral Compositions As Indicators of Ureilite Smelting

Ureilites are very complex rocks, showing evidence of asteroidal melting, cooling, impact disruption, and reaccretion among other processes (Goodrich 1992; Warren and Huber 2006; Downes et al. 2008; Takeda and Yamaguchi 2009). According to Takeda (1987) and Goodrich et al. (2004), molar Fe/Mg versus Fe/Mn of olivine and pyroxene in ureilites can be used to indicate critical aspects of the igneous history of an ureilite. On a plot of molar Fe/Mn versus Fe/Mg (Fig. 3) for monomict (main group) ureilites, olivine-pigeonite and olivine-orthopyroxene ureilites plot on a single trend of near constant, Mn/Mg ratio, which suggests that they are partial melt residues, and are related to one another principally by reduction rather than different degrees of melting (Mittlefehldt 1986; Goodrich et al. 1987a, 1987b; Goodrich and Delaney 2000). On this plot, augite-bearing ureilites lie to right of the residue fit, suggesting that they contain a melt component (Goodrich et al. 2004). In Fig. 3, we plot many olivine analyses from Alma (identifying core compositions) on the Fe/Mn versus Fe/Mg diagram adapted from (Goodrich et al. 2004). The Alma olivines generally follow the residual ureilite Mn/Mg trend, with some displacements to the right that might be explained by the presence of a minor, augite-bearing melt component

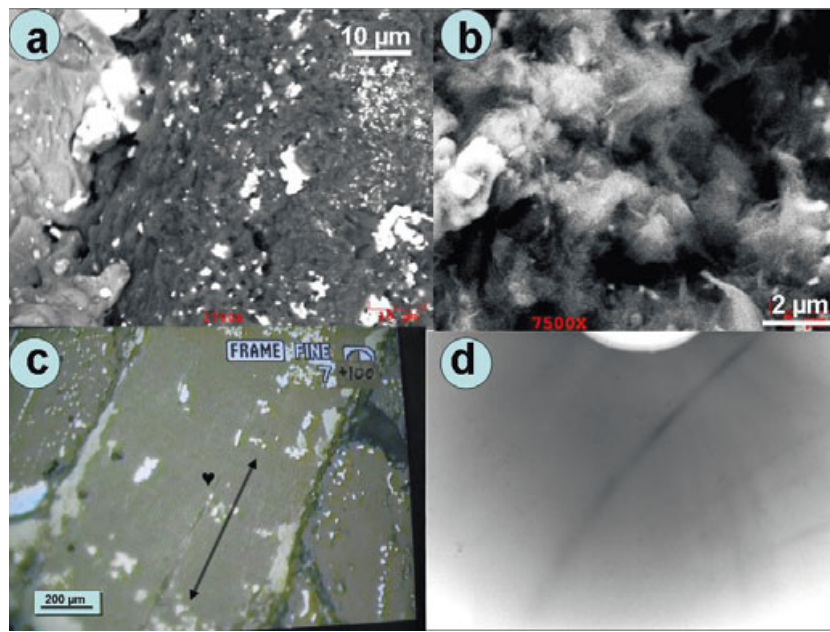


Fig. 12. Carbon in Alma. a) BSE image of graphite (dark gray to the left) in Alma 7. Metal and troilite are white. b) Higher-magnification SEI image from the area shown in (a) showing the flaky texture of this graphite more clearly. c) Reflected light photomicrograph of Alma 4, with the middle of the view occupied by a large crystal of graphite. Cleavage direction is indicated by the arrow. The black heart indicates the position of the SXR pattern in (d). The actual irradiated area is far smaller than the heart, only about 1.5  $\mu\text{m}$  in diameter. d) Laue SXR “single” crystal pattern of the graphite crystal in (c). Despite appearances to the contrary, the dark diffraction maxima arcs reveal this graphite crystal to consist of strongly mosaiced submicron-sized crystallites.

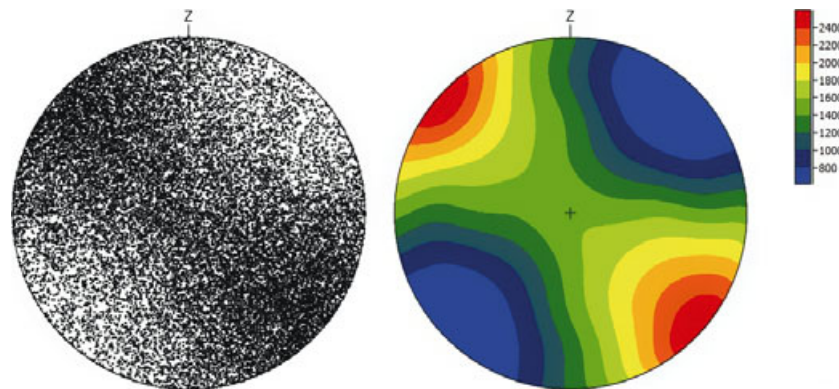


Fig. 13. Visualization of the 3-D preferred orientation of high-Z (metal) grains in Alma stone 7 shows a high degree of preferred orientation. Sample orientation is random. Because of the high porosity, and presumably low degree of impact-related compaction, the foliation origin is related to the genesis of the fragment rather than later tectonic (impact) processing.

(although it should be noted that this component is likely a late shock product, rather than a primary feature such as the Goodrich classification scheme was based on). Alma olivines lie mainly toward the low Fe/Mg (high Fo) portion of the trend, occupied mainly by the olivine-orthopyroxene rather than olivine-pigeonite ureilites. This would be consistent with the classification scheme of Goodrich et al. (2004), as most of the pyroxenes in the Alma samples have  $W_o \leq 5$ . The predominance of pyroxene over olivine in the Alma

samples is also consistent with this classification, as pyroxene/olivine ratio is positively correlated with Fo among main group ureilites (Singletary and Grove 2003; Goodrich et al. 2007), and main group ureilites with  $Fo > 84-86$  all have modal pyroxene > olivine.

The olivines in Alma mainly separate into two fields, roughly on either side of 0.1 molar Fe/Mg, probably a reflection of the polymict nature of Alma. Notice that the augite-bearing monomict ureilites span the entire chondritic Mn/Mg trend, as does Alma.

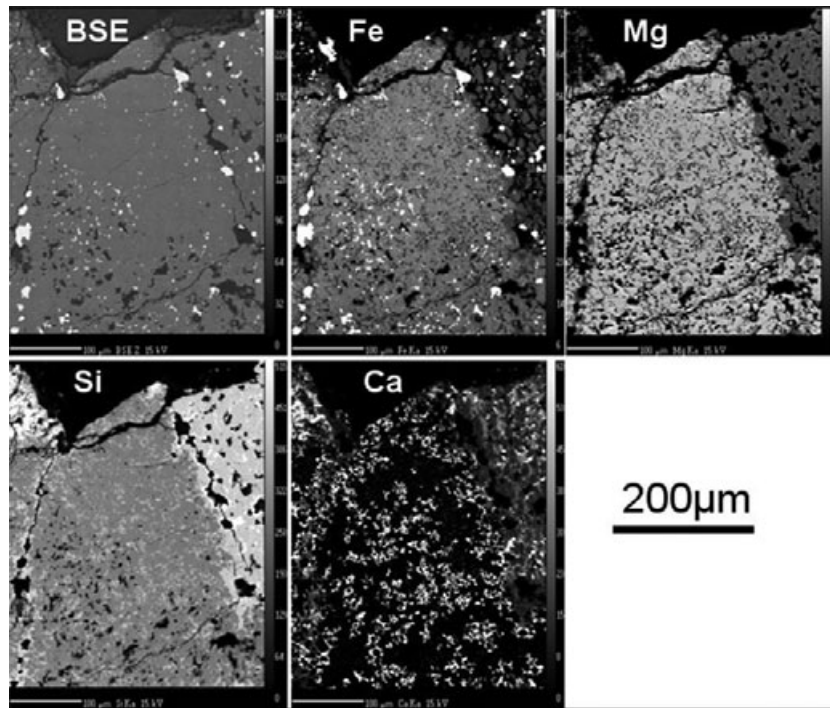


Fig. 14. BSE and element maps of a portion of an olivine-dominated clast in stone 7 (in the center of the image). The location of this clast in the thin section is indicated in Fig. 2. The clast consists mainly of olivine, with interstitial pigeonite and, locally, metal. The scattered, irregular black areas in the BSE image include both pores and carbon. To the right of the clast is some of the reduced pigeonite lithology shown in Fig. 9.

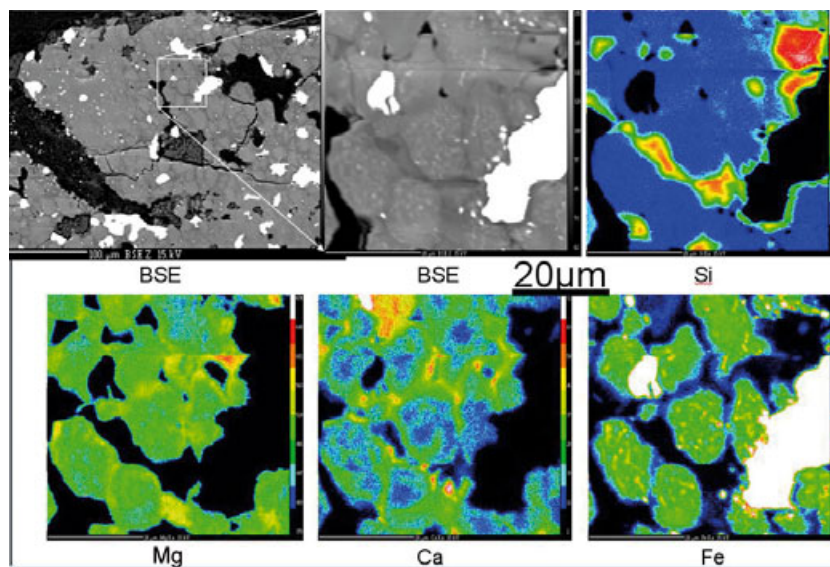


Fig. 15. BSE images and four-element maps of a thoroughly reduced, pyroxene-dominated lithology. The location of this area in the thin section is indicated in Fig. 2. Rounded pigeonite bodies contain nanophase metal, and are surrounded by silica. In the BSE images, carbon is black, metal is white, and interstitial silica is medium gray. The pigeonite bodies are best shown in the Fe map, where they are green and contain nanophase Fe grains (yellow). In the Fe map, large grains of metal are white. The horizontal bar across the upper portions of the images is an artifact of sample charging.

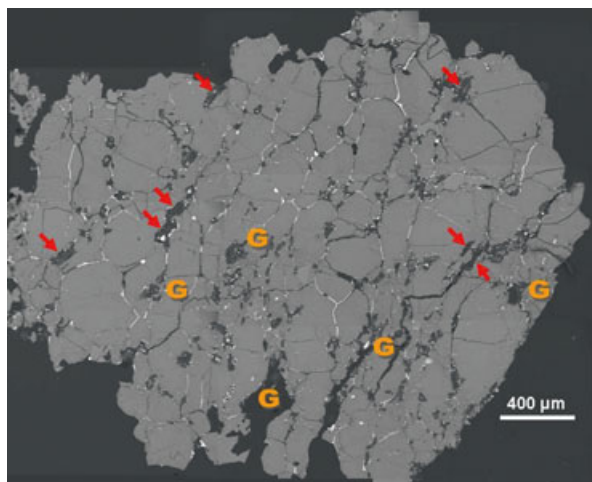


Fig. 16. BSE image of a pyroxene-rich, low-porosity sample—Alma stone 4. The large black areas are carbon (principally graphite, labeled G), and euhedral graphite crystals are arrowed. Metal and sulfide are white. Gray is pyroxene and olivine, principally the former (it is impossible to distinguish them at this contrast level).

Figure 5 shows a histogram of olivine core (i.e., unreduced) compositions (Mg#) for six Alma stones (1, 4, 7, 15, 39, and S138), compared to cores for monomict ureilites (from Mittlefehldt et al. 1998). In this figure, each separate monomict ureilite is shown once, but we have indicated the full range exhibited by Alma olivine cores. The Alma cores are mainly at the high Mg# end of the distribution, away from the distribution peak, although one Alma lithology has core compositions right at the peak position.

Raman spectra of carbon in Alma stone 7 show the grains to be among the most graphitic of any meteorite yet studied with a G-band center and G-band full-width half max of  $1572 \pm 2.1$  and  $42 \pm 5 \text{ cm}^{-1}$  potentially indicating a parent body temperature of  $950 \pm 120 \text{ }^\circ\text{C}$  (Steele et al. 2009; Ross et al. Forthcoming). These carbon aggregates also contain fine-grained troilite and kamacite, the latter containing significant Si and P. Fe-Ni metal is present in all Alma samples, and generally the largest masses are adjacent to carbon masses, suggesting a formation by reduction (Fig. 11) (Herrin et al. 2009, 2010a, 2010b). The metal has a narrow compositional range of  $\text{Fe}_{0.92}\text{Ni}_{0.08}$ – $\text{Fe}_{0.96}\text{Ni}_{0.04}$ , which not only reflects its origin from the reduction of Fe-bearing silicates but also suggests a problem. Generally, smelt-produced metal should have very low Ni. The minor Ni in the Alma metal could have been derived from minor Ni in the precursor silicates, but probably cannot be explained on this basis alone as chondritic olivine and pyroxene typically hold  $<1 \text{ wt}\%$  Ni (Nagahara 1984; Brearley 1993; Klöck and Stadermann 1994; Simon et al. 2002; Weisberg et al. 2004). Some Ni

must have been provided by small Ni-bearing metal melt inclusions which would have been originally present in these silicates.

The clasts which consist entirely of rounded pigeonite grains containing abundant nanophase metal and minute domains of Ca-rich pyroxene (Fig. 15) provide additional information on the smelting event that the ureilite experienced. These rounded pigeonite grains in this lithology are separated by thin (generally  $<10 \text{ }\mu\text{m}$ ) zones of silica, which is mostly amorphous, but is locally crystalline. The origin of these aggregates is undoubtedly related to the reduction event that affected the ureilite as a whole, but here the reduction was complete—rather than merely reduction rims we see completely reduced, small rounded pigeonite bodies.

### Shock and Foliation

Some ureilites are known to exhibit a mosaicized olivine texture similar to Alma, interpreted to result from shock at high temperature, possibly related to the breakup of the ureilite parent body (e.g., Mittlefehldt et al. 1998; Goodrich et al. 2004; Warren and Rubin 2006). Alma has clearly suffered from shock metamorphism (and possibly some melting), as the mosaic silicate texture and presence of diamonds indicate. As is observed in other mosaicized ureilites, the variation in pyroxene compositions in Alma may be due to cation migration during shock (Tribaudino 2006). Even partial melting of silicates might occur as both olivine and pyroxene often show recrystallization textures with small amounts of interstitial Si, Al-rich phases (Figs. 14 and 15). The presence of such interstitial material is found in other ureilites (e.g., Takeda et al. 1989). The Mg-Fe reverse zoning in Alma stone 7 pyroxenes may suggest crystallization during reduction.

Although Alma displays shock metamorphism textures, including mosaicized olivine and deformed pigeonite, the pyroxene compositions are still useful to deduce their thermal history (Herrin et al. 2009, 2010a, 2010b; Mikouchi et al. 2010). The absence of orthopyroxene (*Pbca*) in Alma indicates that the pyroxene equilibration temperature was high, probably higher than  $1300 \text{ }^\circ\text{C}$  (Lindsley 1983; Takeda 1989; Takeda et al. 1989), which is similar to Asuka-881989 (Takeda et al. 2009). The pyroxene composition of Alma stone 7 is similar to the most magnesian ureilites such as ALH 82106 and Northwest Africa 2236 (Takeda et al. 1989). By contrast, silicate compositions of Alma stone 1 are closer to the ferroan ureilites (Downes et al. 2008). Alma stone 1 is especially similar to ALH 81101 because of olivine and pyroxene polycrystalline textures and their compositions,

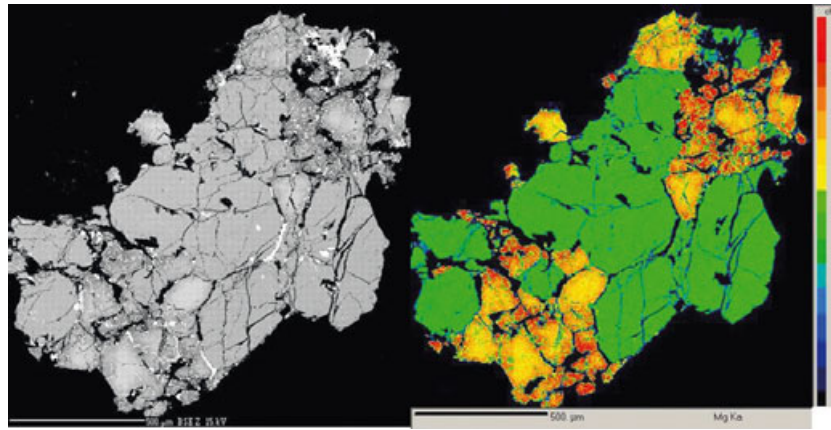


Fig. 17. Alma stone 39—a typical main group ureilite—a combination of pyroxene and zoned olivine, with low porosity. (Left) BSE image of Alma stone 39. The majority of the white phases are metal. Pores and carbon are black. (Right) Mg X-ray element map of Alma stone 39. Pigeonite is green, olivine is yellow ( $\sim\text{Fo}_{87}$ ) to red ( $\sim\text{Fo}_{95}$ ). In this sample, olivine is associated with the highest porosity.

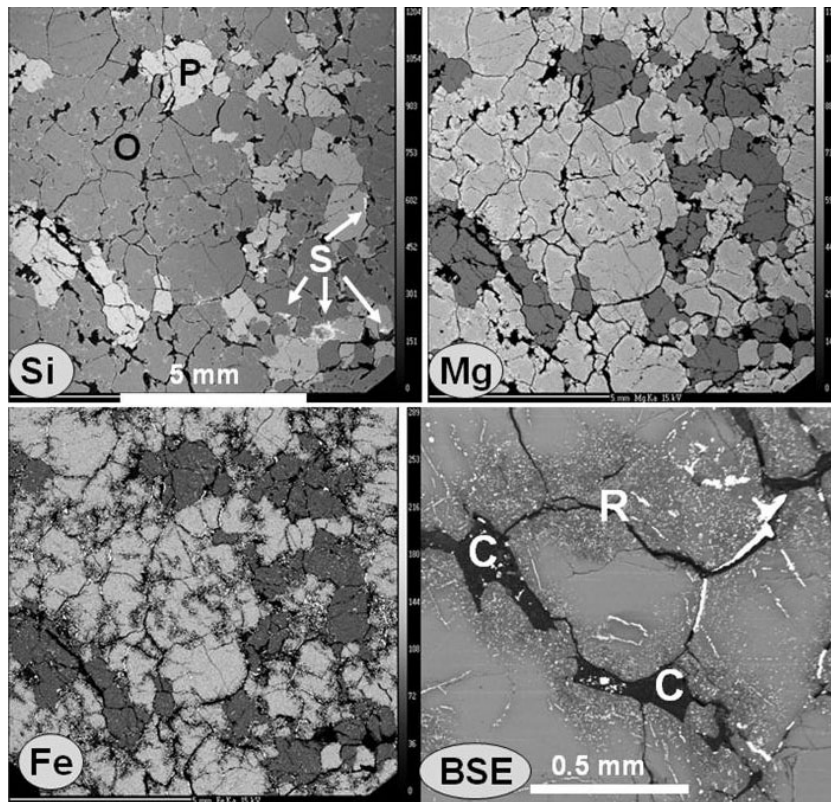


Fig. 18. An olivine-dominated Alma lithology. Shown are three element maps of Alma S138 and one higher-magnification BSE image. In these images, olivine is labeled “O,” pigeonite is “P,” silica is “S,” carbon is “C,” and reduced olivine plus metal is “R.” Fe-Ni metal is white in the Fe and BSE images. It is clear that metal was segregated from olivine adjacent to carbon, probably during high-temperature smelting.

although Alma stone 1 displays a finer-grained texture. These meteorites may share the same origin on the ureilite parent asteroid. Alma stones 7 and 1 represent clasts of two distinct ureilite members, and the coexistence of these two unique members in the same

polymict ureilite indicates a genetic relationship on the same parent asteroid (Downes et al. 2008).

The tomographic study of Alma stone 7 shows a distinct foliation based on the orientation of the metal grains present within it (Fig. 13). Stone 4 does not show

any preferred orientation. Such foliation is known in some ureilites (Goodrich 1992; Mittlefehldt et al. 1998; and references therein) and has been interpreted as being a result of tabular minerals residing in a fluid laminar flow rather than recrystallization and plastic flow. Visualization of the 3-D preferred orientation of high-Z phases (metal) grains in Alma stone 7 shows a high degree of preferred orientation. Synchrotron  $\mu$ CT data were collected at a resolution of 13.5  $\mu$ m per voxel (see Shaddad et al. 2010, for a typical tomogram). Sample orientation is random. Because of the high porosity, and presumably low degree of impact-related compaction, the foliation origin is related to the genesis of the fragment rather than later tectonic (impact) processing. However, a similar analysis of stone 4 high-Z phases does not show evidence of a petrofabric, suggesting again different genetic histories for these two Alma fragments, and that the reaccumulation process of the asteroid (postimpact reaccretion) was heterogeneous in shock stage. Some reaccretion impacts were sufficiently puny that no foliation fabric resulted.

### Pore Fabric

Tomography of Alma reveals that the pores define thin, discontinuous “sheets” connected in three dimensions, suggesting that they outline grains that have been incompletely welded together. Pores have been previously described in other ureilites (Goodrich 1992; Warren and Rubin 2006), but are much more abundant in the porous Alma lithologies than in any other ureilite. The irregular form and 3-D network aspect of the pores suggest that these are not vesicles, and do not outline anything like vesicle cylinders. We suggest that these pore wall olivines are vapor deposits, and if this is true then the compositional similarity to the groundmass core olivines suggests that the pore linings were not formed during the reduction process, and in fact predate it. The fact that the crystals lining the pores are generally euhedral (unlike the groundmass olivine), and do not have the same compositions as the groundmass olivine supports our suggestion that these are vapor-phase deposits.

Therefore Alma may represent an agglomeration of fine-grained, incompletely reduced pellets formed during impact on the ureilite parent asteroid, and subsequently welded together at high temperature. The vapor deposits might have originated from collisions involving the daughter asteroids, but as their compositions are similar to the core compositions of Alma olivine it seems more likely that these pore-lining crystals were deposited *before* the reaccretion of the asteroid. Other Alma samples are similar to typical monomict ureilites, suggesting that asteroid 2008 TC<sub>3</sub> was an agglomerate of

fragments from the original daughter asteroids. Clasts are apparent in some samples, revealing the range of ureilitic materials from diverse locations on the original asteroid that were being thrown together as the asteroid reaccreted. In addition to the stones definitely belonging to the Alma strewn field, we also made microprobe analyses of four totally fusion-crusts, very fresh chondrites that we initially thought had to be unrelated to Alma (stones 16, 25, 41, and A100; see Table 1). These stones proved to be two distinct enstatite and two distinct ordinary chondrites. We think these stones may have been from the same fall as Alma because the stones are very fresh, and the ratio of enstatite to ordinary chondrites is far higher than typical for desert finds (Grady 2000). Bischoff et al. (2010) and Horstmann and Bischoff (2010) reached the same conclusion. The presence of these H5, L4, EH, and EL6 stones found within the Alma strewn field suggests that the final agglomeration of the Alma parent asteroid may have included non-ureilite materials, if it can be shown that all of these materials fell to Earth together (Bischoff et al. 2010; Horstmann and Bischoff 2010; Kohout et al. 2010; Sabbah et al. 2010; Shaddad et al. 2010). In fact, foreign clasts have already often been reported from ureilites, including clasts from CI, ordinary, and R chondrites as well as angrites and ungrouped carbonaceous materials (Brearley and Prinz 1992; Goodrich et al. 2004).

### Comparison to Other Polymict Ureilites

Alma is an anomalous, polymict ureilite (ureilite classification has been verified by oxygen isotope and bulk compositional data (Rumble et al. 2010). Anomalous features include a wide mineralogical range of lithologies, high abundance and large size of pores, crystalline pore wall linings, and overall fine-grained texture, especially for the porous lithology which has the lowest reliable density ever measured in a meteorite. The most notable feature of Alma is that it contains so many different lithologies, as compared with other polymict ureilites (Goodrich et al. 2004; Downes et al. 2008). Thus, while Almahatta Sitta does not contain all previously observed ureilite lithologies (for example, plagioclase-rich materials (Cohen et al. 2004) have not yet been observed in Alma), there is sufficient lithological diversity to suggest that all ureilites *could* derive from a common body, although this is not required by our results.

### CONCLUSIONS

We have identified three main lithologies and several minor ones present as clasts in the Alma meteorite.

The main lithologies are (1) a pyroxene-dominated, very porous, highly reduced lithology; (2) a pyroxene-dominated compact lithology; and (3) an olivine-dominated compact lithology. Although it seems possible that all three lithologies grade smoothly into each other at the kg-scale, at the g-scale this is not apparent in our study of only a few samples of, mainly, subgram masses. The meteorite is a polymict ureilite, with some intriguing features, including exceptionally variable porosity and pyroxene composition. The diversity is so great that one wonders whether more than one ureilite parent asteroid is demanded. The reader is referred to the companion paper by Rumble et al. (2010) for more discussion of this point. Alma stones 7 and 1 represent clasts of two distinct ureilite members, and the coexistence of these two unique members in the same polymict ureilite indicates a probable genetic relationship.

In its various lithologies, Alma bears witness to a rather complete record of the complex history of the ureilite parent asteroid, including asteroidal igneous crystallization, impact disruption, reheating and partial vaporization, high-temperature reduction and carbon burning, and re-agglomeration. Despite considerable work by many investigators, questions remain about this meteorite. It is clear that the generally diverse, fine-grained nature of Alma requires characterization of larger samples than have hitherto been available, to permit us to determine the petrography at a larger scale. However, it is clear that Alma will provide significant new information regarding the geological, especially thermal, history of the ureilite parent asteroid(s), as well as its (their) disruption and reassembly history.

*Acknowledgments*—We are happy to acknowledge the work of the many alert individuals who discovered, observed, tracked, predicted the asteroid landing site, and finally located asteroid 2008 TC<sub>3</sub>. We especially thank the many students of the University of Khartoum who worked hard to recover the final asteroid samples in a harsh environment. None of us had grant funding specifically to support study of Almahata Sitta, but fortunately our grant institutions were lenient for such a fascinating project. Reviews by and other discussions with Makoto Kimura and Paul Warren resulted in a greatly improved manuscript. M. Z. was supported by the Hayabusa Mission and the Stardust Sample Analysis Program. P. J. was supported by a grant from NASA's Planetary Astronomy Program. D. R. thanks NASA for grant NNX07AI48G which supported oxygen isotope analyses.

*Editorial Handling*—Dr. Adrian Brearley

## REFERENCES

- Berkley J. L. 1986. Four Antarctic ureilites: Petrology and observations on ureilite petrogenesis. *Meteoritics* 21:169–189.
- Berkley J. L., Taylor G. J., Keil K., Harlow G., and Prinz M. 1980. The nature and origin of ureilites. *Geochimica et Cosmochimica Acta* 44:1579–1597.
- Bischoff A., Horstmann M., Laubenstein M., and Haberger S. 2010. Asteroid 2008 TC<sub>3</sub>—Almahata Sitta: Not only a ureilitic meteorite, but a breccia containing many different achondritic and chondritic lithologies (abstract #1763). 41st Lunar and Planetary Science Conference. CD-ROM.
- Brearley A. J. 1993. Matrix and fine-grained rims in the unequilibrated CO<sub>3</sub> chondrite, ALHA77307: Origins and evidence for diverse, primitive nebular dust components. *Geochimica et Cosmochimica Acta* 57:1521–1550.
- Brearley A. and Prinz M. 1992. CI chondrite-like clasts in the Nilpena polymict ureilite: Implications for aqueous alteration processes in CI chondrites. *Geochimica et Cosmochimica Acta* 56:1373–1386.
- Britt D. and Consolmagno G. 2004. Meteorite porosities and densities: A review of trends in the data (abstract #2108). 35th Lunar and Planetary Science Conference. CD-ROM.
- Cohen B., Goodrich C., and Keil K. 2004. Feldspathic clast populations in polymict ureilites: Stalking the missing basalts from the ureilite parent body. *Geochimica et Cosmochimica Acta* 68:4249–4266.
- Deer W., Howie R., and Zussman J. 1978. *Single-chain silicates, rock-forming minerals*, vol. 2A. The Geological Society, Essex, England, 668 p.
- Downes H., Mittlefehldt D. W., Kita N. T., and Valley J. W. 2008. Evidence from polymict ureilite meteorites for a disrupted and re-accreted single ureilite parent asteroid gardened by several distinct impactors. *Geochimica et Cosmochimica Acta* 72:4825–4844.
- Franchi I., Sexton A., Wright I. P., and Pillinger C. 1998. Oxygen isotopic homogeneity in the ureilite population (abstract #1685). 28th Lunar and Planetary Science Conference. CD-ROM.
- Friedrich J. M., Wignarajah D. P., Chaudhary S., Rivers M. L., Nehru C. E., and Ebel D. S. 2008. Three-dimensional petrography of metal phases in equilibrated L chondrites—Effects of shock loading and dynamic compaction. *Earth and Planetary Science Letters* 275:172–180.
- Goehner R. P. and Michael J. R. 1996. Phase identification in a scanning electron microscope using backscattered electron Kikuchi patterns. *Journal of Research of National Institute of Standards and Technology* 101:301–308.
- Goodrich C. A. 1992. Ureilites: A critical review. *Meteoritics* 27:327–352.
- Goodrich C. A. and Delaney J. S. 2000. Fe/Mg-Fe/Mn relations of meteorites and primary heterogeneity of achondrite parent bodies. *Geochimica et Cosmochimica Acta* 64:149–160.
- Goodrich C. A., Jones J., and Berkeley J. 1987a. Origin and evolution of the ureilite parent magmas: Multi-stage igneous activity on a large parent body. *Geochimica et Cosmochimica Acta* 51:2255–2273.
- Goodrich C. A., Keil K., Berkley J. L., Laul J. C., Smith M. R., Wacker J. F., Clayton R. N., and Mayeda T. K. 1987b. Roosevelt County 027—A low-shock ureilite with interstitial silicates and high noble gas concentrations. *Meteoritics* 22:191–218.

- Goodrich C. A., Scott E. R. D., and Fioretti A. M. 2004. Ureilitic breccias: Clues to the petrologic structure and impact disruption of the ureilite parent asteroid. *Chemie der Erde* 64:283–327.
- Goodrich C. A., Van Orman J. A., and Wilson L. 2007. Fractional melting and smelting on the ureilite parent body. *Geochimica et Cosmochimica Acta* 71:2876–2895.
- Grady M. 2000. *Catalogue of meteorites*, 5th ed. Cambridge: Cambridge University Press. pp. 11–36.
- Herrin J., Zolensky M., Ito M., Jenniskens P., and Shaddad M. 2009. Fossilized smelting; reduction textures in the Almahata Sitta ureilite (abstract). *Meteoritics & Planetary Science* 44:A89.
- Herrin J., Ito M., Zolensky M., Mittlefehldt D., Jenniskens J., and Shaddad M. 2010a. Thermal history and fragmentation of ureilitic asteroids; insights from the Almahata Sitta fall (abstract 1095). 41st Lunar and Planetary Science Conference. CD-ROM.
- Herrin J., Zolensky M., Ito M., Le L., Mittlefehldt D., Jenniskens P., and Shaddad M. 2010b. Thermal and fragmentation history of ureilitic asteroids; insights from the Almahata Sitta fall. *Meteoritics & Planetary Science* 45. This issue.
- Horstmann M. and Bischoff A. 2010. Characterization of spectacular lithologies from the Almahata Sitta breccia (abstract #1784). 41st Lunar and Planetary Science Conference. CD-ROM.
- Hudon P., Romanek C., Paddock L., and Mittlefehldt D. W. 2004. Evolution of the ureilite parent body (abstract #2075). 35th Lunar and Planetary Science Conference. CD-ROM.
- Hutchison R. 2004. *Meteorites. A petrologic, chemical and isotopic synthesis*. Cambridge University Press. 506 p.
- Ivanov A. V., Zolensky M. E., Saito A., Ohsumi K., MacPherson G. J., Yang S. V., Kononkova N. N., and Mikouchi T. 2000. Florenskyite, FeTiP, a new phosphide from the Kaidun meteorite. *American Mineralogist* 85:1082–1086.
- Jenniskens P., Shaddad M., Numan D., Elsir S., Kadoda A., Zolensky M., Le L., Robinson G. A., Friedrich J., Rumble D., Steele A., Chesley S., Fitzsimmons A., Duddy S., Hsieh H., Ramsay G., Brown P., Edwards W., Tagliaferri E., Boslough M., Spalding R., Dantowitz R., Kozubal M., Pravec P., Borovička J., Charvat Z., Vaubaillon J., Kuiper J., Albers J., Bishop L., Mancinelli R., Sandford S., Milam S., Nuevo M., and Worden S. 2009. The impact and recovery of asteroid 2008 TC<sub>3</sub>. *Nature* 458:485–488.
- Ketcham R. A. 2005. Computational methods for quantitative analysis of three dimensional features in geological specimens. *Geosphere* 1:32–41.
- Ketcham R. A. and Carlson W. D. 2001. Acquisition, optimization and interpretation of X-ray computed tomographic imagery: Applications to the geosciences. *Computers & Geosciences* 27:381–400.
- Klöß W. and Stadermann F. J. 1994. Mineralogical and chemical relationships of interplanetary dust particles, micrometeorites and meteorites. In *Analysis of interplanetary dust*, edited by Zolensky M. E., Wilson T. L., Rietmeijer F. J. M., and Flynn G. J. AIP Press. pp. 51–87.
- Kogure T. 2003. A program to assist Kikuchi pattern analysis. *Journal of the Crystallographic Society of Japan* 45:391–395. (in Japanese with English abstract: the program is available at <http://www-gbs.eps.s.u-tokyo.ac.jp/kogure/edana>).
- Kohout T., Jenniskens P., Shaddad M. H., and Haloda J., 2010. Inhomogeneity of asteroid 2008 TC<sub>3</sub> (Almahata Sitta meteorites) revealed through magnetic susceptibility measurements. *Meteoritics & Planetary Science* 45. This issue.
- Lindsley D. H. 1983. Pyroxene thermometry. *American Mineralogist* 68:477–493.
- Mason B. 1962. *Meteorites*. USA: J. Wiley and Sons, Inc. New York, NY. pp. 111–112.
- Mikouchi T., Zolensky M., Ohnishi I., Suzuki T., Takeda H., Jenniskens P., and Shaddad M. 2010. Transmission electron microscopy of pyroxenes in the Almahata Sitta ureilite. *Meteoritics & Planetary Science* 45. This issue.
- Mittlefehldt D. W. 1986. Fe-Mg-Mn relations of ureilite olivines and pyroxenes and the genesis of ureilitites. *Geochimica et Cosmochimica Acta* 50:107–110.
- Mittlefehldt D. W., McCoy T. J., Goodrich C. A., and Kracher A. 1998. Non-chondritic meteorites from asteroidal bodies. In *Planetary materials*, edited by Papike J. Reviews in Mineralogy, vol. 36. Mineralogical Society of America, Washington, D.C. pp. 4.1–4.195.
- Nagahara H. 1984. Matrices of type 3 ordinary chondrites—Primitive nebular records. *Geochimica et Cosmochimica Acta* 48:2581–2595.
- Ross A., Steele A., Fries M., Kater L., Downes H., Jones A., Smith C., Jenniskens P., Zolensky M., and Shaddad M. Forthcoming. MicroRaman spectroscopy of diamond and graphite in Almahata Sitta and comparison with other ureilitites. *Meteoritics & Planetary Science*. 45.
- Rumble D., Zolensky M., Friedrich J., Jenniskens P., and Shaddad M. 2010. The oxygen isotope composition of Almahata Sitta. *Meteoritics & Planetary Science* 45. This issue.
- Sabbah H., Morrow A. L., Jenniskens P., Shaddad M. H., and Zare R. N. 2010. Polycyclic aromatic hydrocarbons in asteroid 2008 TC<sub>3</sub>: Dispersion of organic compounds inside asteroids. *Meteoritics & Planetary Science* 45. This issue.
- Scott E., Taylor J., and Keil K. 1993. Origin of ureilite meteorites and implications for planetary accretion. *Geophysical Research Letters* 20:415.
- Shaddad M. H., Jenniskens P., Numan D., Kudoda A. M., Elsir S., Riyad I. F., Elkareem A., Alameen M., Alameen N. M., Eid O., Osman A. T., AbuBaker M. I., Chesley S. R., Chodas P. W., Albers J., Edwards W. N., Brown P. G., Kuiper J., and Friedrich J. M. 2010. The recovery of asteroid 2008 TC<sub>3</sub>. *Meteoritics & Planetary Science* 45. This issue.
- Simon S., Davis A., Grossman L., and McKeegan K. 2002. A hibonite-corundum inclusion from Murchison: A first generation condensate from the solar nebula. *Meteoritics & Planetary Science* 37:533–548.
- Singletary S. J. and Grove T. L. 2003. Early petrologic processes on the ureilite parent body. *Meteoritics & Planetary Science* 38:95–108.
- Steele A., Fries M., Jenniskens P., and Zolensky M. 2009. Characterisation of diamond in the Almahata Sitta meteorite (abstract #9.08). Division of Planetary Sciences—Astronomical Association of America Society, American Astronomical Society, Washington, D.C. Annual Meeting.
- Takeda H. 1987. Mineralogy of Antarctic ureilitites and a working hypothesis for their origin and evolution. *Earth and Planetary Science Letters* 81:358–370.

- Takeda H. 1989. Mineralogy of coexisting pyroxenes in magnesian ureilites and their formation conditions. *Earth and Planetary Science Letters* 93:181–194.
- Takeda H. and Yamaguchi A. 2009. Decomposed pigeonite in Antarctic ureilites and the thermal history of the parent body. *Proceedings of the NIPR Symposium on Antarctic Meteorites* 32:68–69.
- Takeda H., Mori H., and Ogata H. 1989. Mineralogy of augite-bearing ureilites and the origin of their chemical trends. *Meteoritics* 24:73–81.
- Takeda H., Yamaguchi A., and Mikouchi T. 2009. Low-calcium pigeonite in Northwest Africa and Asuka ureilites with reference to planetary processes (abstract). *Meteoritics & Planetary Science* 44:A200.
- Tribaudino M. 2006. Microtextures and crystal chemistry of pigeonite in the ureilites ALHA77257, RKPA80239, Y-791538 and ALHA81101. *Meteoritics & Planetary Science* 41:979–988.
- Tribaudino M., Pasqual D., Mollin G., and Secco L. 2003. Microstructures and crystal chemistry in P2<sub>1</sub>/c pigeonites. *Mineralogy and Petrology* 77:161–176.
- Warren P. H. 2010. Ureilites: Pigeonite thermometry and the unimportance of pressure-buffered smelting during evolution as asteroidal mantle restites (abstract #1530). 41st Lunar and Planetary Science Conference. CD-ROM.
- Warren P. H. and Huber H. 2006. Ureilite petrogenesis: A limited role for smelting during anatexis and catastrophic disruption. *Meteoritics & Planetary Science* 41:835–849.
- Warren P. H. and Rubin A. 2006. Melted-reduced pigeonite, vermicular silica, Si-rich glasses, and other impact smelting products in the LAR 04315 ureilite (abstract). *Meteoritics & Planetary Science* 41:A184.
- Warren P. H., Ulf-Moeller F., Huber H., and Kallemeyn G. W. 2006. Siderophile geochemistry of ureilites: A record of early stages of planetesimal core formation. *Geochimica et Cosmochimica Acta* 70:2104–2126.
- Weisberg M., Connolly H., and Ebel D. 2004. Petrology and origin of amoeboid olivine aggregates in CR chondrites. *Meteoritics & Planetary Science* 39:1741–1753.
- Wilson L. W., Goodrich C. A., and Van Orman J. A. 2008. Thermal evolution and physics of melt extraction on the ureilite parent body. *Geochimica et Cosmochimica Acta* 72:6154–6176.
- Zolensky M., Nakamura K., Gounelle M., Mikouchi T., Kasama T., Tachikawa O., and Tonui E. 2002. Mineralogy of Tagish Lake: An ungrouped type 2 carbonaceous chondrite. *Meteoritics & Planetary Science* 37:737–761.
-